10.2514/6.2016-1955

AIAA SciTech Forum
4-8 January 2016, San Diego, California, USA
57th AIAA/ASCE/AHS/ASC Structures, Structural Dynamics, and Materials Conference

Strain State Estimation of Very Flexible Unmanned Aerial Vehicle

Zi Yang Pang* and Carlos E. S. Cesnik†
The University of Michigan, Ann Arbor, MI 48105-2410

This paper presents two different methods for estimating wing shape and rigid body attitude using displacement (stereovision reconstruction) and orientation information (inertia measurement units) at discrete points along a very flexible wing. First, theoretical relationship between the system states (strain, strain rate, body velocity, attitude etc.) and the sensor measurements are derived. Using the derived relationship, a nonlinear least squares fit is developed to obtain wing shape snapshots as well as rigid body attitude. The second method employs a Kalman filter to obtain both shape and rate information. The first method is more accurate since it employs nonlinear strain-displacement relationship at the cost of higher computational cost. However, in the presence of noise in the sensor measurement, the Kalman filter is faster and performs better in terms of accuracy.

Nomenclature

β	=	linear and angular velocity of the vehicle
ε	=	strain states column vector
ε_x, κ_x, κ_y, κ_z	=	components of strain (extensional and three orthogonal bending)
κ_{max}	=	maximum curvature
λ	=	inflow states
$\dot{\Theta}$	=	angular velocity at sensor location
Φ, θ, ψ	=	Euler angles
ζ	=	quaternions
ω	=	angular velocity
σ	=	variance
b_{span}	=	wing semi-span
d	=	displacement magnitude
dp	=	displacement vector from a reference point
f, g, h	=	generic functions (discrete time)
$h(s)$	=	nodal position and orientation
p_w	=	position of an element node in body frame
p_p	=	position of arbitrary point in body frame
q	=	generic first-order states
q_0, q_1, q_2, q_3	=	components of quaternions
r_ζ, r_ε, r_v	=	error metric for quaternions, strain and displacement
t_k	=	k^{th} time step
v	=	linear velocity
v_{k+1}	=	Kalman filter residual of estimated and measured states
w_x, w_y, w_z	=	directrix column vectors
$\hat{x}_{k\|k}$, $\hat{x}_{k+1\|k}$	=	Kalman filter estimated states
y_{obsv}	=	output column vector of sensor measurements
A_d, B_d, C_d, D_d	=	linearized state space matrices
C^{Bw}	=	rotation matrix from beam to body frame
$C^{ww'}$	=	rotation matrix from beam to auxiliary frame

* PhD Candidate, (pziyang@umich.edu), Department of Aerospace Engineering. Member, AIAA
† Professor, (cesnik@umich.edu), Department of Aerospace Engineering. Fellow, AIAA

C^{BG}	=	rotation matrix from inertial to body frame
C_{FF}, C_{FB}, C_{BF}, C_{BB}	=	generalized damping matrices
F, G, H	=	generic function (continuous time)
F_1, F_2, F_3	=	inflow matrices
$I_{n\times n}$	=	identity matrix of size n by n
J	=	structural jacobian matrices
K_{FF}	=	stiffness matrix
M_{FF}, M_{FB}, M_{BF}, M_{BB}	=	generalized mass matrices
$P_{k\|k}$, $P_{k+1\|k+1}$	=	error covariance matrix
P_B	=	inertial position of the B reference frame
Q	=	process noise covariance matrix
R	=	sensor noise covariance matrix
R_B, R_F	=	generalized loads
U	=	linear column velocity vector
W	=	weighting matrix
$\{.\}_B$	=	column vector expressed in body frame
$\{.\}_w$	=	column vector expressed in local beam frame
$\{.\}_G$	=	column vector expressed in global inertial frame

I. Introduction

The desire to reduce fuel burn due to commercial and environmental pressures (e.g., reducing direct operating cost in civilian aviation) and/or operational reasons (e.g., longer endurance for prolonged surveillance in military applications) drives the design of next generation aircraft. Such designs often employ high aspect ratio wings for aerodynamic efficiency and light weight structures to reduce total weight. As a result, these designs tend to exhibit large wing deformation within normal operating envelope. In addition, the low vibrational structural frequencies often interact with classical flight dynamics modes. Aircraft with these characteristics are termed Very Flexible Aircraft (VFA). Design of control systems for VFA requires consideration of coupled aeroelastic dynamics with the additional challenge that the dynamics itself are state-dependent and non-linear in nature.[1,2]

From the controls perspective, the assumptions of structurally rigid, linear, time invariant (LTI) description, typically used for traditional aircraft analysis are no longer valid.[3,4] Many work done on VFA flight control system typically requires feedback of elastic structural information and/or its time derivative. Some examples are strain states,[5–7] mode shapes and amplitude[8,9] or elastic displacements.[10] There is an implicit assumption that such information will be available and provided. There are many engineering challenges in sensor placement and selection (due to weight, volume and power constraints) to provide such information in an accurate and timely manner. In practical applications, it is unlikely that all the feedback states will be measured, and the most common approach to this problem in literature is to design an observer to perform state estimation from some output measurements.[5,10–12]

Although there are attempts to perform state estimation from displacement information (such as from vision-based system),[12,13] as well as accelerometers or inertia measurement units (IMU),[14,15] there is little published literature in sensor fusion of both displacement and IMU data. Vision-based measurement methods are typically limited by the update rate (~1−5Hz) due to 1) relatively long image processing duration and 2) bandwidth limitation in sending video data from the cameras to image processing unit. IMU, on the other hand, has high update rate (~20−100Hz) and more easily embedded in the aircraft structure. However, IMU suffer from drift and bias, and time integration of noisy rate measurements gives unbounded error on the displacement.

At the University of Michigan's Active Aeroelasticity and Structures Research Laboratory, much research is conducted on the theoretical aeroelastic modeling of VFA as well as flight control design of such vehicle. An aeroelastic test vehicle X-HALE[16] has been built and fully instrumented for experimental verification of modeling fidelity and real world flight test of research control design.

This paper explores state estimation employing two different methods: 1) nonlinear least squares and 2) Kalman Filter (KF) fusing vision-based displacement information as well distributed IMU sensor information. The hardware as well as the post processing software architecture for the stereovision system have been developed in previous work.[17]

II. Theoretical Formulation

The geometrically-nonlinear, strain-based aeroelastic state space equations used are first presented. Next, the relationship between measurements and the system states are derived. Finally, two methods are presented to recover the deformed shape. The first employs a nonlinear least-square method and returns the "instantaneous" shape at the current snapshot. The second employs a Kalman filter and returns both static and dynamic estimations for position and motion.

A. Strain-based Coupled Aeroelastic Formulation

Cesnik and co-workers[1,6] have developed a non-linear coupled aeroelastic toolbox UM/NAST to perform simulations of VFA. In this formulation, the frame is defined as wing right (+x), towards wing leading edge (+y) and normal to beam surface (+z) as shown in Figure 1.

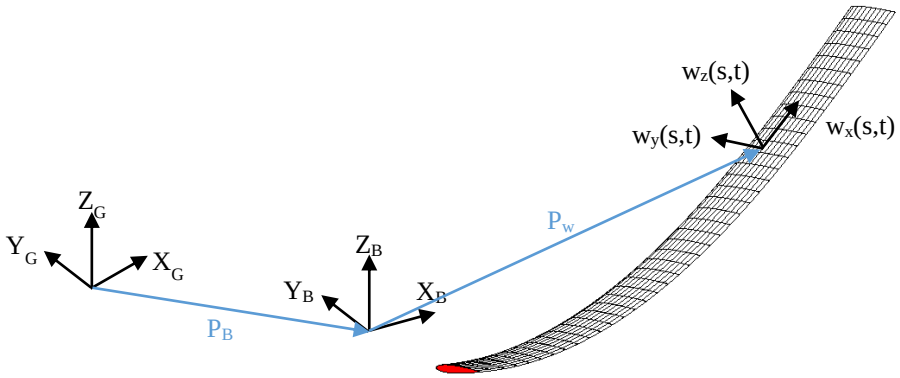

Figure 1. Coordinate Frame definition.

Each beam element has three nodes with four degrees of freedom: extensional, twist and two orthogonal bending strain of the beam reference line. The strain vector within each beam element is assumed constant and is denoted by

$$\varepsilon_e = \begin{bmatrix} \varepsilon_x & \kappa_x & \kappa_y & \kappa_z \end{bmatrix}^T \tag{1}$$

The position and orientation of each point can be described by a position vector and three directrix vectors, resulting in 12 components. For a point at location *s* from the origin along the wing, one has:

$$h(s) = \begin{bmatrix} p_w(s) & w_x(s) & w_y(s) & w_z(s) \end{bmatrix}^T \tag{2}$$

The rigid body motion of the body frame origin is described by the three linear and three angular velocities, denoted by

$$\beta = \begin{bmatrix} v_B & \omega_B \end{bmatrix}^T \tag{3}$$

Given nodal directrix vectors $\left(w_x, w_y, w_z\right)$, the direction cosine matrix C^{Bw} from the local beam frame *w* to the body frame *B* can be expressed as:

$$C^{Bw} = \begin{bmatrix} w_x & w_y & w_z \end{bmatrix} \tag{4}$$

which implies that an arbitrary column vector $\{u\}_w$ expressed in the beam reference frame can be transformed to the body frame by:

$$\{u\}_B = C^{Bw}\{u\}_w \tag{5}$$

The position and orientation $h(s)$ can be recovered from the strain ε_e and boundary condition h_0 using the kinematic relationship,

$$h(s) = e^{K(s-s_0)}h_0 = e^{G(s)}h_0 \tag{6}$$

where

$$K = \begin{bmatrix} 0 & 1+\varepsilon_x & 0 & 0 \\ 0 & 0 & \kappa_z & -\kappa_y \\ 0 & -\kappa_z & 0 & \kappa_x \\ 0 & \kappa_y & -\kappa_x & 0 \end{bmatrix}_{12\times 12} \tag{7}$$

Nodal displacement can then be computing by marching Eq. (6) from root to tip between connecting beam elements. Finally, the coupled aeroelastic equations of motion can be expressed as:[1]

$$\begin{bmatrix} M_{FF}(\varepsilon) & M_{FB}(\varepsilon) \\ M_{BF}(\varepsilon) & M_{BB}(\varepsilon) \end{bmatrix} \begin{Bmatrix} \ddot{\varepsilon} \\ \dot{\beta} \end{Bmatrix} + \begin{bmatrix} C_{FF}(\varepsilon,\dot{\varepsilon},\beta) & C_{FB}(\varepsilon,\dot{\varepsilon},\beta) \\ C_{BF}(\varepsilon,\dot{\varepsilon},\beta) & C_{BB}(\varepsilon,\dot{\varepsilon},\beta) \end{bmatrix} \begin{Bmatrix} \dot{\varepsilon} \\ \beta \end{Bmatrix} + \begin{bmatrix} K_{FF} & 0 \\ 0 & 0 \end{bmatrix} \begin{Bmatrix} \varepsilon \\ b \end{Bmatrix} = \begin{Bmatrix} R_F(\varepsilon,\dot{\varepsilon},\ddot{\varepsilon},\beta,\dot{\beta},\lambda,\zeta,u) \\ R_B(\varepsilon,\dot{\varepsilon},\ddot{\varepsilon},\beta,\dot{\beta},\lambda,\zeta,u) \end{Bmatrix} \tag{8}$$

$$\dot{\zeta} = -\frac{1}{2}\Omega_\zeta(\beta)\zeta \tag{9}$$

$$\dot{P}_B = \begin{bmatrix} C^{GB}(\zeta) & 0 \end{bmatrix} \beta \tag{10}$$

$$\dot{\lambda} = F_1 \begin{Bmatrix} \ddot{\varepsilon} \\ \dot{\beta} \end{Bmatrix} + F_2 \begin{Bmatrix} \dot{\varepsilon} \\ \beta \end{Bmatrix} + F_3 \lambda \tag{11}$$

The inflow states in Eq. (11) will be neglected for what follows. Recasting Eq. (8)−(10) as a first order system with states $q = \begin{bmatrix} \varepsilon, \dot{\varepsilon}, \zeta, \beta, P_B \end{bmatrix}$ and control input *u*,

$$\begin{aligned} \dot{q} &= F(q,u) \\ y &= H(q) \end{aligned} \tag{12}$$

Linearization of Eq. (8)−(11) are also derived by Su and Cesnik.[1] Subscript 0 denotes that the matrices are evaluated at some reference trim condition, and superscript tilde (~) denotes the perturbation of the states from the reference condition, i.e.,

$$\begin{aligned} \dot{\tilde{q}} &= \left.\frac{\partial F}{\partial q}\right|_{q_0,u_0} \tilde{q} + \left.\frac{\partial F}{\partial u}\right|_{q_0,u_0} \tilde{u} \\ \tilde{y} &= \left.\frac{\partial H}{\partial q}\right|_{q_0,u_0} \tilde{q} \end{aligned} \tag{13}$$

Eq. (13) can be converted (using various integration schemes) to obtain discrete time state space equations.

$$\tilde{q}_{k+1} = A_d \tilde{q}_k + B_d \tilde{u}_k \tag{14}$$

$$\tilde{y}_{k+1} = C_d \tilde{q}_k \tag{15}$$

B. Relationship between System States *q* and Measurements from Sensors

System states are rarely directly provided by the sensor measurements. However, system states can be indirectly computed using kinematics and/or strain-based formulation shown in Section II.A. This section will present the output equations relating sensor measurements and system states.

1. Output Equation for Center Mounted Inertia Navigation System (INS)

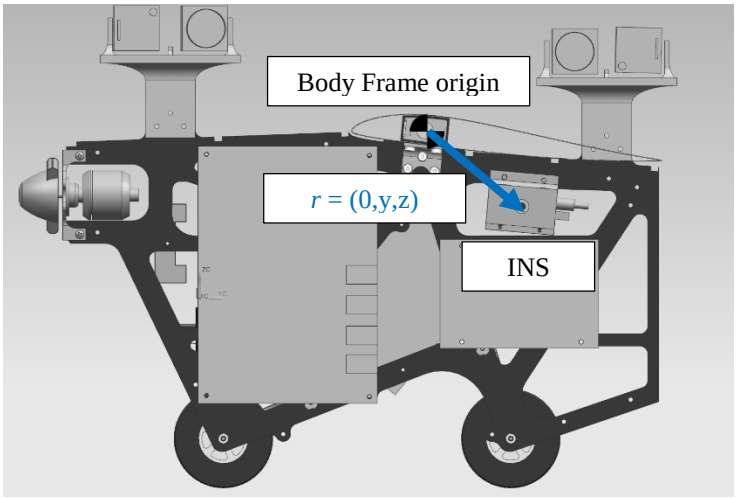

Figure 2. Relationship between body frame origin and INS mounting location in body frame.

Consider an inertial navigation system unit mounted near the center of the aircraft to provide "rigid body" measurements. The coordinate frame can usually be aligned to the body frame by software calibration in most INS units. The available output measurements are:

1. $\dot{\Theta}_B$ -- three component angular rate (p,q,r) in the body frame
2. U_B -- three component linear velocity (u,v,w) in the body frame
3. ϕ_B, θ_B, ψ_B -- Euler angles relating inertial and body frame
4. P_B -- Inertial position (X_G, Y_G, Z_G)

The output equations relating system states to measurements are

$$\dot{\Theta}_B = \begin{bmatrix} 0_{3\times3} & I_{3\times3} \end{bmatrix} \beta \tag{16}$$

$$U_B = \begin{bmatrix} I_{3\times3} & r_{INS}^{\times} \end{bmatrix} \beta \tag{17}$$

where r_{INS} represents the offset between the INS mounting location and the body origin (Figure 2). The superscript cross denotes a cross product matrix (where a cross product between two vectors is expressed as a matrix multiplication):

$$a^{\times} = \begin{bmatrix} 0 & -a_3 & a_2 \\ a_3 & 0 & -a_1 \\ -a_2 & a_1 & 0 \end{bmatrix} \tag{18}$$

The direction cosine matrix relating inertial and body coordinate frame using Yaw-Pitch-Roll rotation sequence can computed using[18]

$$\begin{aligned} C^{BG} &= \begin{bmatrix} \cos\theta\cos\psi & \cos\theta\sin\psi & -\sin\theta \\ \sin\phi\sin\theta\cos\psi - \cos\phi\sin\psi & \sin\phi\sin\theta\sin\psi + \cos\phi\cos\psi & \sin\phi\cos\theta \\ \cos\phi\sin\theta\cos\psi + \sin\phi\sin\psi & \cos\phi\sin\theta\sin\psi - \sin\phi\cos\psi & \cos\phi\cos\theta \end{bmatrix} \\ &= \begin{bmatrix} q_0^2 + q_1^2 - q_2^2 - q_3^2 & 2(q_1q_2 + q_0q_3) & 2(q_1q_3 - q_0q_2) \\ 2(q_1q_2 - q_0q_3) & q_0^2 - q_1^2 + q_2^2 - q_3^2 & 2(q_2q_3 + q_0q_1) \\ 2(q_1q_3 + q_0q_2) & 2(q_2q_3 - q_0q_1) & q_0^2 - q_1^2 - q_2^2 + q_3^2 \end{bmatrix} \end{aligned} \tag{19}$$

To relate Euler angles to quaternions,[18]

$$\phi_B = \tan^{-1}\left(\frac{2q_2q_3 + 2q_0q_1}{q_0^2 - q_1^2 - q_2^2 + q_3^2}\right)$$
$$\theta_B = -\sin^{-1}\left(2q_1q_3 - 2q_0q_2\right) \tag{20}$$
$$\psi_B = \tan^{-1}\left(\frac{2q_1q_2 + 2q_0q_3}{q_0^2 + q_1^2 - q_2^2 - q_3^2}\right)$$

2. Output Equation for Outboard Inertial Measurement Unit (IMU)

Consider an IMU rigidly mounted somewhere on the aircraft flexible wing. Moreover, assume that the IMU frame is aligned with the local beam frame *w*. The available measurements are:

1. $\dot{\Theta}_w$ -- three component angular rate (*p*,*q*,*r*) in the local beam frame
2. ϕ_w, θ_w, ψ_w -- Euler angles relating inertial and local beam frame

The output equation for the angular rates at the IMU location is given by

$$\dot{\Theta}_w = C^{wB}\left(J_{\theta\varepsilon}\dot{\varepsilon} + J_{\theta\beta}\beta\right) \tag{21}$$

where $\dot{\Theta}_w$ denotes three component angular rate in the local beam frame, $C^{wB} = \left(C^{Bw}\right)^T$ is the direction cosine matrix relating the body to local beam frame, and $J_{\theta\beta}, J_{\theta\varepsilon}, J_{p\beta}, J_{p\varepsilon}$ are appropriate rows of the structural jacobians derived by Su and Cesnik[1] (Eq. 5 and Eq. 6). There will be a problem with computing the Euler angle from inertial to local beam frame using direction cosine C^{wB} when the IMU is pointing vertically down due to gimbal lock. Hence, an auxiliary frame w' is defined. With that direction cosine matrix relating the inertial frame to the auxiliary frame is given by

$$C^{w'G} = C^{w'w}C^{wB}C^{BG} \tag{22}$$

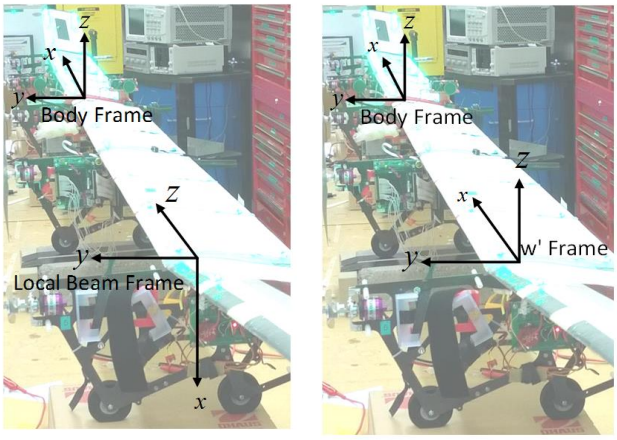

Figure 3. Local beam frame (left) and auxiliary frame (right). *The frame is simply rotated about the y-axis by 90 degrees.*

The Euler angle (for Yaw-Pitch-Roll rotation sequence) can be computed using

$$\begin{aligned}\phi_w &= \tan^{-1}\left(\frac{C_{23}^{w'G}}{C_{33}^{w'G}}\right)\\ \theta_w &= -\sin^{-1}\left(C_{13}^{w'G}\right)\\ \psi_w &= \tan^{-1}\left(\frac{C_{12}^{w'G}}{C_{11}^{w'G}}\right)\end{aligned} \tag{23}$$

where C_{ij} represents the (i, j) component of the direction cosine matrix C.

3. Output Equation for Stereovision (SV) System

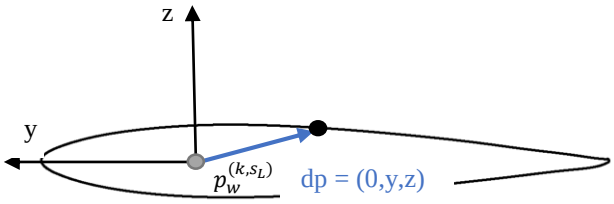

Figure 4. Arbitrary point on the cross-section from beam reference axis in the local beam frame.

For a flexible wing modeled using finite elements, a position and orientation of a point $h^{(k,s_L)}$, s_L position along the on the k^{th} element, is given by

$$h^{(k,s_L)} = e^{G(s_L)}h^{(k,0)} \tag{24}$$

where $h^{(k,0)}$ is the nodal position and rotation at node 0 of the k^{th} element. For any arbitrary point p on the airfoil cross-section, its position in the body frame is given by

$$p_p = \begin{bmatrix} I_{3\times3} & 0_{9\times9}\end{bmatrix} h^{(k,s_L)} + C^{Bw}dp \tag{25}$$

where dp represents the position of an arbitrary point from the beam reference axis intersection with the given cross section (see Figure 4).

C. Nonlinear Least Squares Formulation (NLS)

In this formulation, strain states ε and quaternions ζ are estimated based on various measurements. This method only provides wing shape and body orientation at a given time step. Dynamic states will not be estimated. Moreover, considering the expected drift in yaw measurements from an IMU, only the pitch and roll readings are used.

First, the observed sensor measurements (from center mounted INS, M distributed outboard IMU and N SV markers) using Eq. (16)−Eq. (25) are stacked into a column vector, that is:

$$y_{obsv} = \begin{bmatrix}\phi_B & \theta_B & \psi_B & \theta_{w1} & \phi_{w1} & \cdots & \theta_{wM} & \phi_{wM} & p_{p1} & \cdots & p_{pN}\end{bmatrix}^T \tag{26}$$

Note that the H function in Eq. (12) will be a nonlinear function in terms of only strains and quaternions. Therefore, this estimation is formulated as a nonlinear least squares problem where the 2-norm squared error between predicted distance and observed distance is minimized.

$$\min_{\varepsilon,\zeta}\left(\left\|W\left(y_{obsv} - H(\zeta,\varepsilon)\right)\right\|_2\right)^2 \tag{27}$$

W is a user-specified weighting matrix. This matrix can be used to tune the sensitivity of the least square solution to each sensor type. For example, one may wish to place less emphasis on a noisy sensor compared to a less noisy one from a higher-grade sensor. To avoid solving a constrained optimization problem for the quaternion estimation, Eq. (27) can be converted to Euler angle representation and solved for three Euler angles directly. The solution to Eq. (27) is obtained using MATLAB® `lsqnonlin`. In order to obtain an overdetermined solution, the following inequality on each wing must be adhered to:

$$2M + 3N > 4n_{el} \tag{28}$$

where n_{nel} is the number of beam finite elements on each wing. Overdetermined system will be better at noise rejection. Regardless, MATLAB® `lsqnonlin` is capable of solving an undetermined system as well.

D. Kalman Filter (KF) Formulation

Kalman filter[19] is an algorithm which combines noisy measurements to give an optimal estimate of the states of a dynamical system. Consider the following discrete time linear model,

$$\begin{aligned} x_{k+1} &= A_d x_k + B_d u_k + B_d w_k \\ y_k &= C_d x_k + v_k \end{aligned} \tag{29}$$

where $w_k \sim N(0, Q)$ is the process noise and $v_k \sim N(0, R)$ is the measurement noise. $N(0, v)$ denotes a Gaussian distribution with mean zero and variance v. The optimal estimate of the system states is given by the prediction and update steps. In the prediction step, using usual notation,[20]

$$\hat{x}_{k+1|k} = A_d \hat{x}_{k|k} + B_d u_k \tag{30}$$

$$P_{k+1|k} = A_d P_{k|k} A_d^T + B_d Q_k B_d^T \tag{31}$$

In the update step,

$$v_{k+1} = y_{k+1} - H_{k+1} x_{k+1|k} \tag{32}$$

$$P_{k+1|k+1} = \left[I - K_{k+1} H_{k+1} \right] P_{k+1|k} \tag{33}$$

$$\hat{x}_{k+1|k+1} = \hat{x}_{k+1|k} + K_{k+1} v_{k+1} \tag{34}$$

$$K_{k+1} = P_{k+1|k} H_{k+1}^T \left[H_{k+1} P_{k+1|k} H_{k+1}^T + R^{-1} \right] \tag{35}$$

where

$$H_{k+1} = C_{d\Delta} \tag{36}$$

The size of H_{k+1} is dependent on the size of $C_{d\Delta}$, which is the relevant rows of the output matrix C_d (given by Eq. (29)) at the $k+1$ time step. In this formulation, the update of the estimated states can be done with any subset of measurement signals. This is typically the case as IMU and SV data have different update rates. In derivation of H_{k+1}, some simplifying assumptions are made. Although the jacobian matrices $J_{\theta\beta}, J_{\theta\varepsilon}, J_{p\beta}, J_{p\varepsilon}$ are functions of strain ε, they are assumed to be constant at the evaluated $\varepsilon_{k|k}$ (the current deformed shape). This assumption holds for small perturbations to the system.[1] For the KF formulation, the angular rates instead of the Euler angles are used as output measurements, i.e.,

$$y_{obsv} = \begin{bmatrix} \dot{\Theta}_B & U_B & \dot{\Theta}_{w1} & \cdots & \dot{\Theta}_{wM} & p_{p1} & \cdots & p_{pN} \end{bmatrix}^T \tag{37}$$

III. Numerical and Experimental Setup

E. X-HALE Test Vehicle Description

X-HALE[16] is a flexible, high-aspect-ratio, wing-boom-tail type aircraft. It has a 6-m span (constructed with 6 identical 1-m sections) with constant 0.2-m chord. There is one center pod and four outboard pods housing electronics and batteries. All-movable horizontal tails are attached to the outboard pods. The center tail is capable of switching only between horizontal and vertical orientations to provide additional yaw stability when needed. Four VectorNav VN−100* IMUs are mounted in the outboard pods and a Microrobotics MIDG-II† INS is mounted on the center pod. Four PointGrey Flea3‡ cameras are mounted above the center pod to provide SV displacement measurement for both wings. High power LEDs (18 on each wing) are placed at specific location on the top wing surface and act as visual markers. Figure 5 shows the sensor location and distribution on X-HALE. The SV system

* http://www.vectornav.com/

† http://www.microboticsinc.com/MIDG_INS-GPS.htm

‡ http://ww2.ptgrey.com/USB3/Flea3

on X-HALE provides position at the 36 target marker location $\left(p_{p1}, \cdots, p_{p36} \right)$ in the camera coordinate system. This information is then post processed so that the measured outputs are in the body frame.

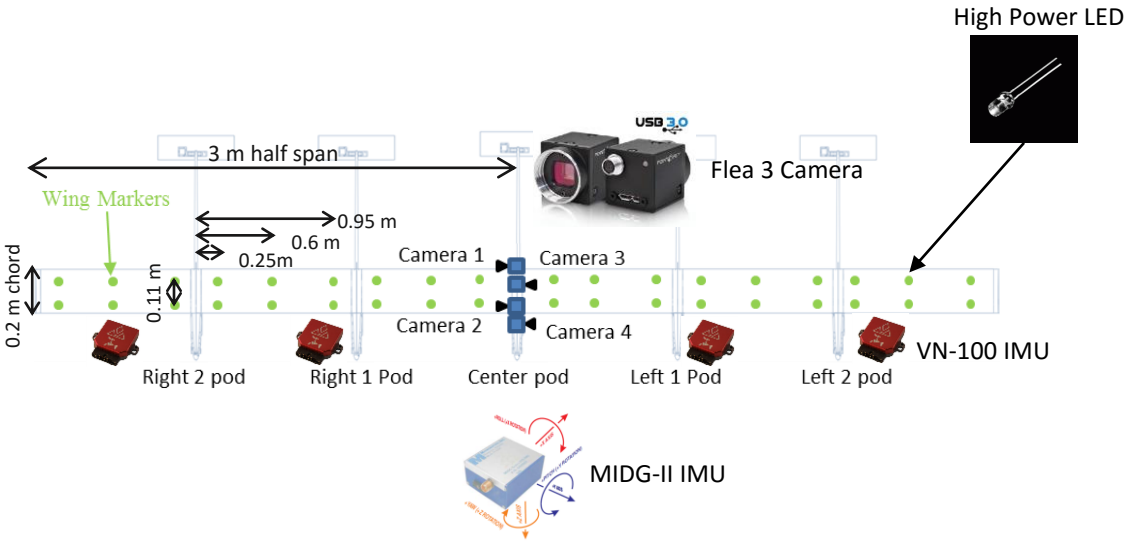

Figure 5. X-HALE flight test sensor schematic.

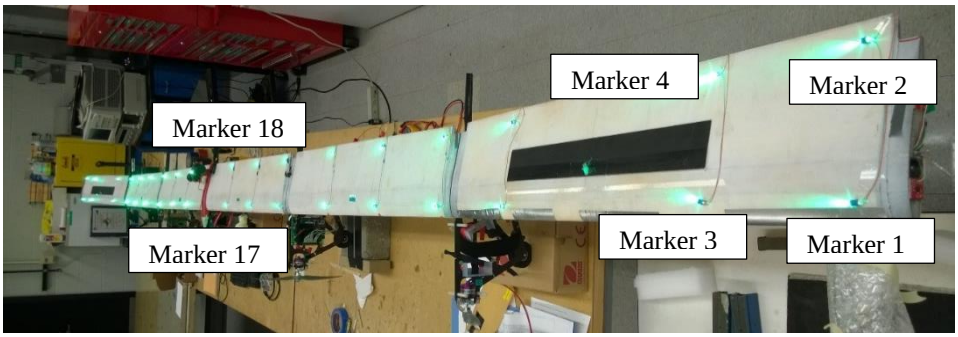

Figure 6. X-HALE flight test vehicle with LED powered on (pictured without tail). *The markers are labelled from wing tip to wing root, leading edge to trailing edge.*

The SV setup and processing algorithm has been described in previous work.[17] Images captured are stored in solid state devices (SSD) as raw 8-bit greyscale images at 25Hz. Currently, image processing is done off-line using a desktop PC. VN-100 measurements are captured at 50Hz and Microbotics MIDG-II measurements are captured at 50Hz.

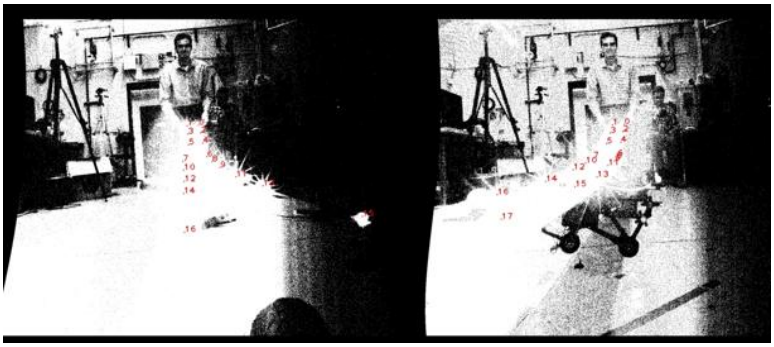

Figure 7. Marker detection and triangulation superimposed on image. *The exposure of the image is increased artificially for illustration purposes.*

The numerical model of X-HALE in UM/NAST is shown in Figure 8. Each inboard 1-meter wing segment is modelled using two flexible finite elements, the outboard dihedrals are also modelled using two flexible elements, while the pods, booms and tails are modelled using one rigid element. This model has a total of 48 elastic variables, six linear and angular velocity states, four quaternions and three inertial position components.

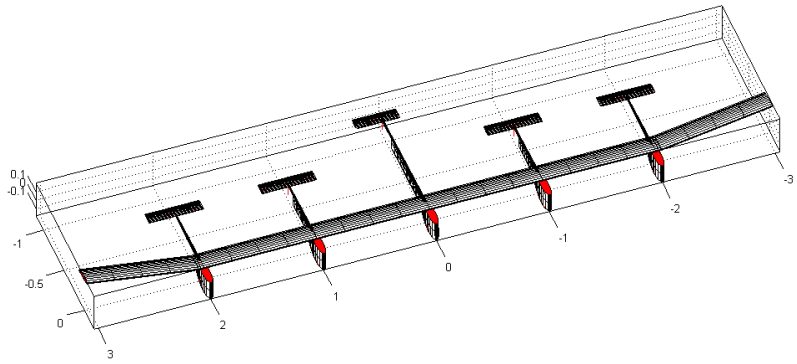

Figure 8. UM/NAST X-HALE model.

F. Vicon Benchmark Description

A Vicon system was used to independently measure the wing shape using a different set of Vicon infra-red (IR) markers. These IR markers are placed at known locations on the top wing surface and most of them close to the LED markers. A set of 12 Vicon T-40[*] cameras are placed around the X-HALE test vehicle to provide good reconstruction of the IR markers at all times (Figure 9). The IR markers displacements, post-processed via Vicon Blade[†] software, serve as a benchmark to verify the accuracy of the sensors on X-HALE (e.g., Figure 10).

Figure 9. Vicon IR makers (left) and Vicon camera positioning (right).

Time varying forces are applied to the wing tips by hand to obtain dynamic structural information. The forces are applied such that the wing experiences deformation in all three directions (twist and bending in two planes).

[*] http://www.vicon.com/System/TSeries
[†] http://www.vicon.com/Software/Blade

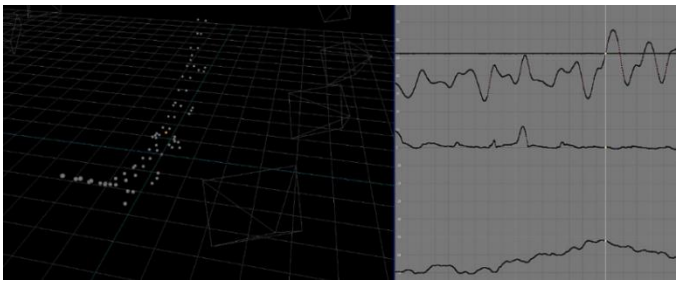

Figure 10. Vicon IR marker reconstruction in Blade software. *Trace shows the marker displacement due to dynamic tip load.*

G. Benchmark Cases

To validate the state estimation formulation, one experimental and three numerical test cases will be used (Table 1 and Table 2, respectively). For the experimental test case, force and moments are applied by hand to displace the wing and the corresponding displacements are obtained using the Vicon system. In the numerical test cases, wing shape are obtained from UM/NAST dynamic simulations. The sensor measurements are simulated. In the three numerical test cases, the wing is modelled as a cantilevered beam, and the loading conditions produce out-of-plane, twisting and in-plane bending deformations, respectively. The load is applied at the beam reference axis at the wing tip (Figure 11).

Table 1. Experimental benchmark case

Test Case	Source	Sensor Readings	Load
1	Vicon	Vicon measurement	Not measured. Forces and moments applied by hand

Table 2. Numerical benchmark cases

Test Case	Source	Sensor Readings	Load
2	UM/NAST	Simulated in software	10N, 1Hz sine tip force in z direction (out-of-plane bending)
3	UM/NAST	Simulated in software	10Nm, 1Hz sine tip moment in x direction (twist)
4	UM/NAST	Simulated in software	20N, 1Hz sine tip force in y direction (in-plane bending)

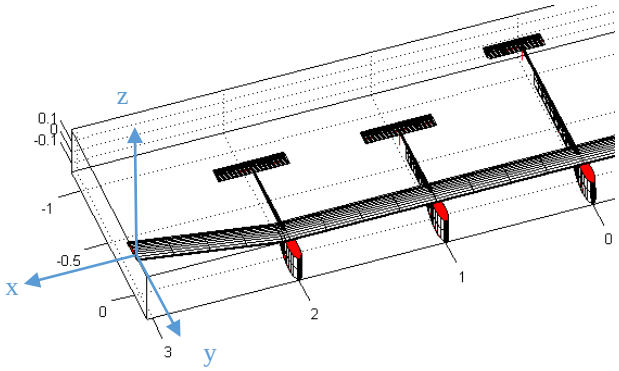

Figure 11. Benchmark cases load application direction and location. *The loads are applied at the beam reference axis in the body fixed frame.*

IV. Results

In this section, the sensor accuracy is first determined based on Vicon experimental benchmark. Then, results for NLS and KF, with and without sensor noise are presented. In addition, three different sensor combinations are tested to determine their performance. Each sensor combination has advantages and disadvantages in terms of power, weight and space requirements. The sensor combinations are: 1) INS/IMU 2) INS/SV 3) INS/IMU/SV.

A. X-HALE Instrumentation Accuracy

First, the accuracy of the sensors is examined to establish the baseline measurement noise using Test Case 1. The displacement of a given point is taken as the difference between its current deformed position and its undeformed position, that is, the distance travelled by that point. The recovered displacement of Marker 1 is compared against the Vicon benchmark in Figure 12. The error is defined to be the difference between the Vicon measured displacements and the SV measured displacements at each time instant, normalized by the X-HALE semispan. The mean error between SV results and Vicon is 7.7 ± 5.1mm (< 0.25% of semi-span). The error is dependent approximately linearly on the distance away from the camera.

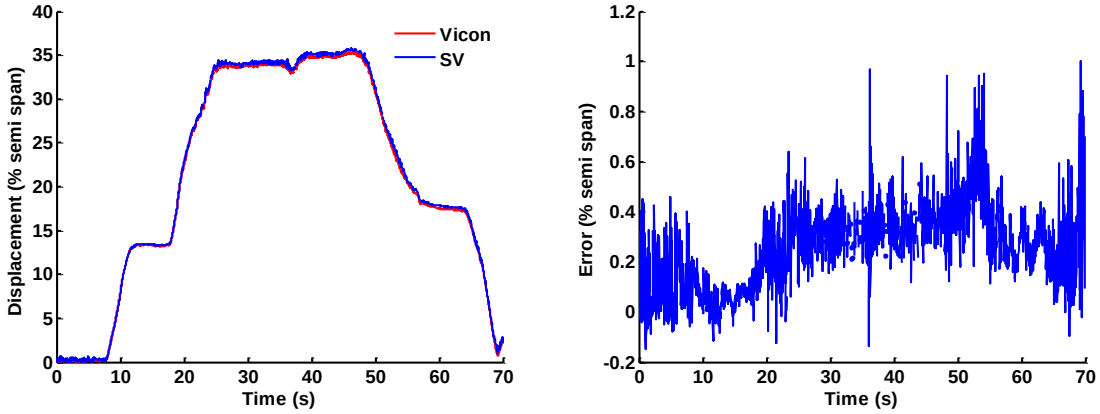

Figure 12. Comparison between reconstructed displacement of Marker 1 against Vicon Benchmark

The accuracy of the VN-100 IMU is also good in twist (-1.05 ± 0.7 degrees) and out-of-plane bending (-1.9 ± 1.9 degrees) degrees of freedom. Figure 13 confirmed that yaw measurements from the VN-100 are unreliable. This is attributed to electro-magnetic (EM) interference with the magnetometer from surrounding electronics housed in the pods, as well as a large EM disturbance generated by the brushless DC motors.

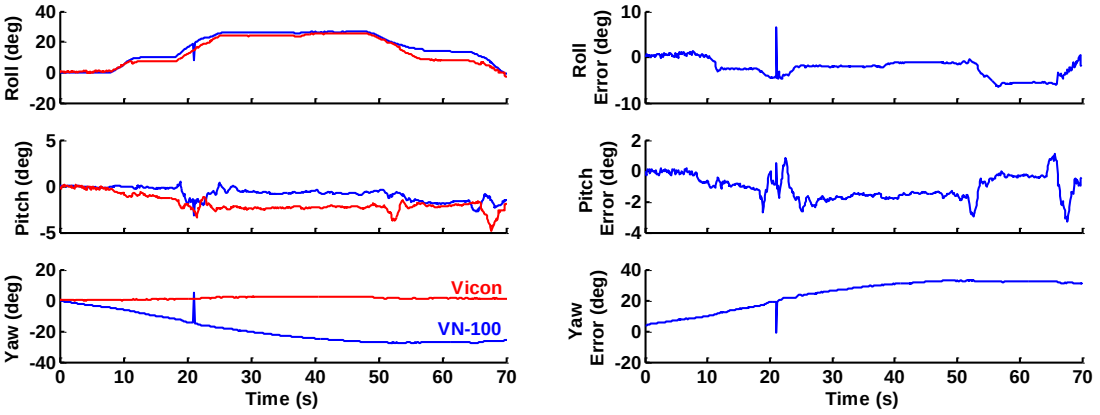

Figure 13. Comparison between VN-100 orientation measurement of leftmost pod against Vicon Benchmark

In the subsequent numerical benchmark, noise is added to simulated sensor readings to reflect real world conditions (Table 3). The added noise level is a conservative estimate based on the benchmark above and manufacturer's datasheet.

Table 3. X-HALE instrumentation noise levels

Sensor Type	Noise Level	Remarks
Stereovision LED markers	1 mm for Marker Pair 17, 18 9 mm for Marker Pair 1, 2	Noise varies linearly with distance from camera.
MIDG	2 deg for angles 2 deg/s for angular rate 0.5 m/s for velocity	MIDG-II specification datasheet*
VN-100	2 deg for angles 2 deg/s for angular rate	VN-100 specification datasheet**

* http://www.microboticsinc.com/Support.htm

** http://www.vectornav.com/products/vn100-rugged/specifications

B. Nonlinear Least Squares Accuracy

With no noise added, and giving equal weights to all measurements, the quality of the nonlinear least square fit for each time step is measured based on the residue defined in Eq. (38). The residue is then averaged over the entire time history, i.e.,

$$r_\varepsilon(t_k) = \frac{1}{n}\sum_{i=1}^{n}\left(\frac{\kappa_{x,NLS}(t_k)-\kappa_{x,true}(t_k)}{\kappa_{true,max}} + \frac{\kappa_{y,NLS}(t_k)-\kappa_{y,true}(t_k)}{\kappa_{true,max}} + \frac{\kappa_{z,NLS}(t_k)-\kappa_{z,true}(t_k)}{\kappa_{true,max}}\right)$$

$$r_\varsigma(t_k) = \frac{1}{3}\left(\left(\phi_{NLS}(t_k)-\phi_{true}(t_k)\right)+\left(\theta_{NLS}(t_k)-\theta_{true}(t_k)\right)+\left(\psi_{NLS}(t_k)-\psi_{true}(t_k)\right)\right) \quad (38)$$

The strains are normalized by the maximum curvature $\kappa_{true,\max}$ over the entire time history. Strain residue can be thought of as the fractional fit error compared to maximum strain observed. Note that INS/IMU combination results in an undetermined system, the solution is a least-norm solution with respect to Eq. (38), INS measurements are simply propagated. Similarly, elastic displacement and rigid body angles are decoupled in INS/SV combination, the INS measurements will also be "passed through" in NLS solution. Hence, the error in fitted results for rigid body angles for both cases are reported under INS only.

Figure 14 shows that when sensors are not corrupted by noise, NLS using INS/IMU/SV performs very well. The recovered strains and hence recovered deformations are identical to that of the analytical solution. Table 5 shows that the INS/IMU combination is worst at strain estimation in terms of recovering strain with or without noise except for Test Case 3. This is because the INS/IMU combination is poor at recovering wing in-plane bending deformation (Figure 15). This is expected as in-plane strain is lost when yaw measurements are discarded. Therefore, it is clear that INS/IMU is not sufficient for state-estimation when in-plane deformation is significant.

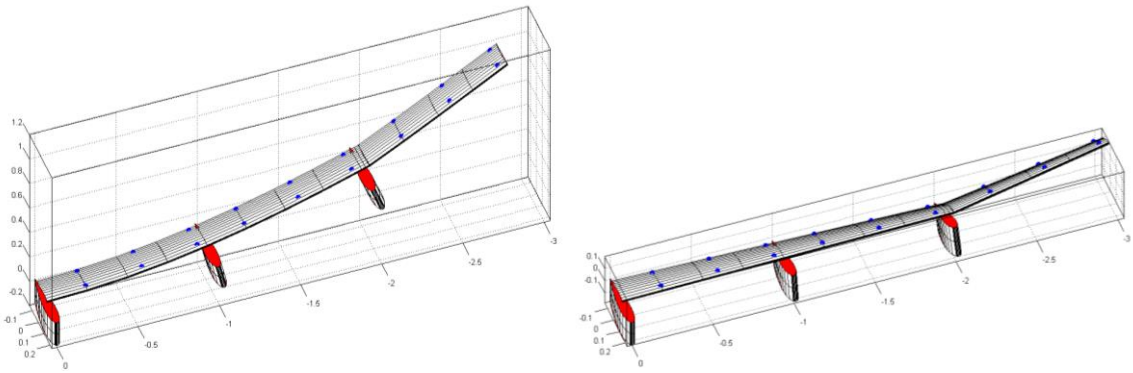

Figure 14. Strain states estimation with no noise using all measurements for Test Case 2 and 3. *The fitted wing shape is plotted with the SV markers (denoted in blue spheres) from the numerical benchmark. They are in excellent agreement.*

In the presence of noise, the accuracy using SV measurements drastically worsen (Figure 16). This suggests that the strain is very sensitive to noise in displacement measurements. Combining all three sensor measurements produces less residue than INS/SV or INS/IMU alone. Hence, it can be concluded that INS/IMU/SV combination will provide the best estimation. Since the displacement is built from the root to the tip, one may expect that the

error in strain will accumulate when marched outboard. However, results shows that the fit error does not accumulate in the NLS formulation.

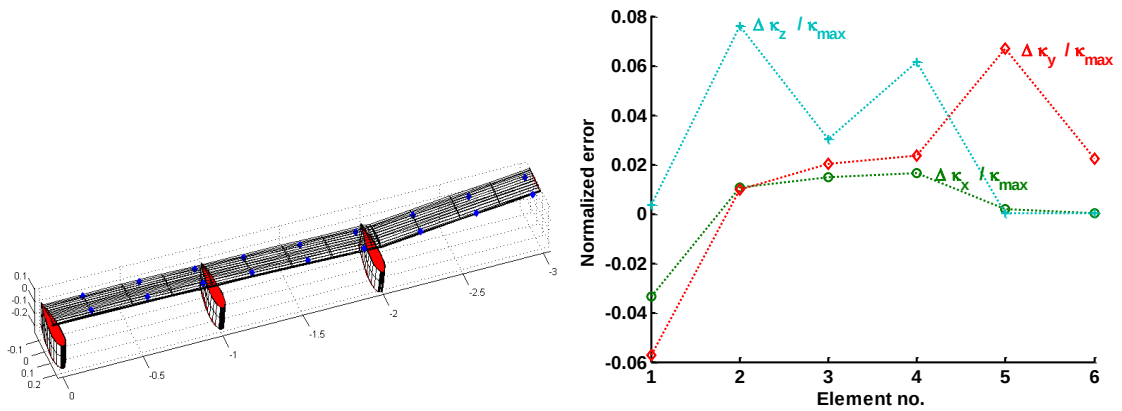

Figure 15. INS/IMU is poor at capturing in-plane deformation. *Notice how the actual position of the SV markers (blue sphere) indicate that the wing should be bending forward. The error in strain is also higher.* $\kappa_{max} = 0.1530$.

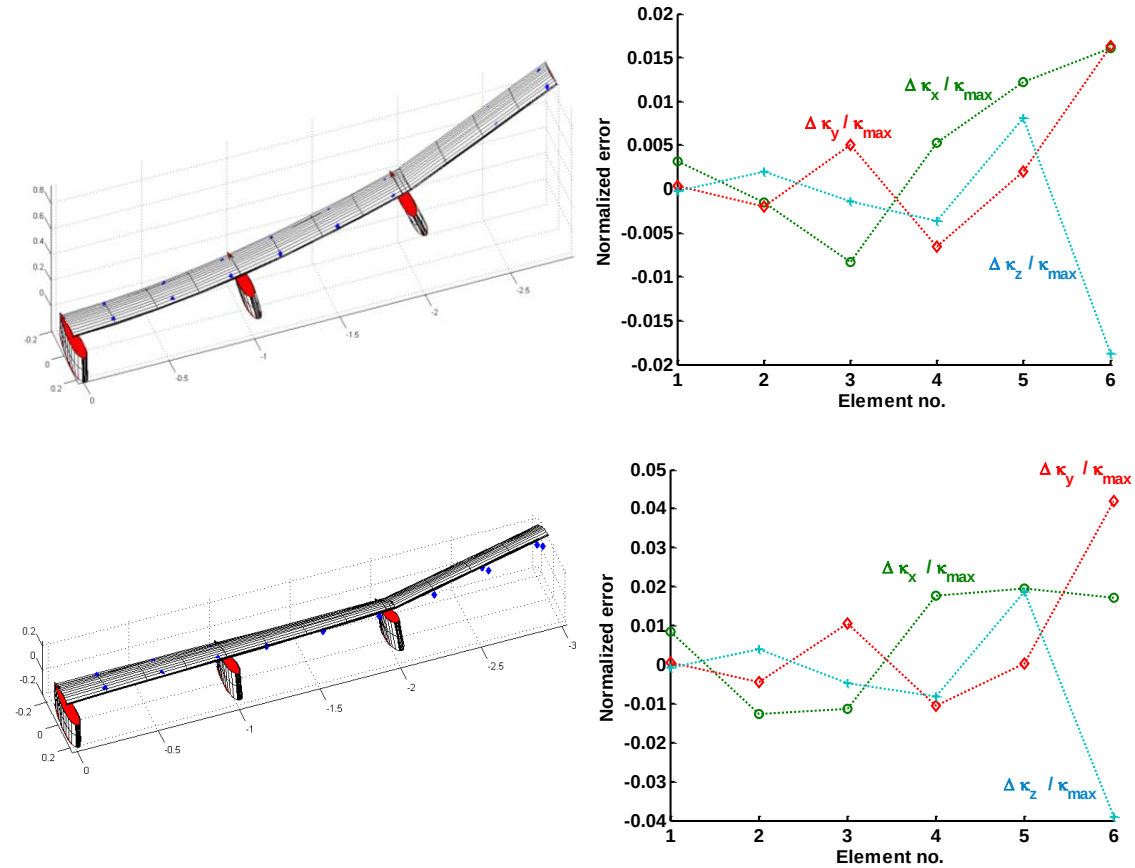

Figure 16. Strain states estimation with noise using INS/SV for Test Case 2 (top) and 3 (bottom). *A snapshot of fitted wing shape is plotted with the SV markers (denoted in blue spheres) from the numerical benchmark. Measurement noise clearly corrupts the NLS fitted strain. The mean residue is plotted on the right. The elements are numbered from wing root to wing tip.* $\kappa_{max} = 0.437$ *(Test Case 2).* $\kappa_{max} = 0.188$ *(Test Case 3).*

Table 4. Euler angle residue r_ζ comparison using NLS with various combinations of measurement sources.

Underlined cells indicate sensor combination with lowest residue.

Measurement	Test Case 2 (w/o noise)	Test Case 2 (with noise)	Test Case 3 (w/o noise)	Test Case 3 (with noise)	Test Case 4 (w/o noise)	Test Case 4 (with noise)
INS	–	-5.954×10^{-4}	–	$\underline{-5.954\times10^{-4}}$	–	-5.954×10^{-4}
INS/IMU/SV	9.883×10^{-10}	$\underline{-5.006\times10^{-4}}$	-1.581×10^{-9}	-5.957×10^{-4}	1.909×10^{-9}	$\underline{-4.923\times10^{-4}}$

Table 5. Strain residue r_ε comparison using NLS with various combination of measurement sources.

Underlined cells indicate sensor combination with lowest residue.

Measurement	Test Case 2 (w/o noise)	Test Case 2 (with noise)	Test Case 3 (w/o noise)	Test Case 3 (with noise)	Test Case 4 (w/o noise)	Test Case 4 (with noise)
INS/SV	4.904×10^{-8}	1.550×10^{-3}	1.914×10^{-8}	2.585×10^{-3}	9.002×10^{-8}	4.424×10^{-3}
INS/IMU	3.336×10^{-3}	-3.768×10^{-3}	2.093×10^{-3}	$\underline{-5.778\times10^{-4}}$	1.687×10^{-2}	1.485×10^{-2}
INS/IMU/SV	$\underline{2.825}\times10^{-8}$	$\underline{1.364\times10^{-3}}$	$\underline{1.398\times10^{-8}}$	2.229×10^{-3}	$\underline{3.491\times10^{-8}}$	$\underline{3.482\times10^{-3}}$

Typically, the solution converges in about 10 iterations. The time taken to solve each snapshot is approximately 5−20 seconds on a desktop computer (Intel i7 2.0GHz) without providing analytical jacobians (derivative of Eq. (27)) and approximately 0.5−3 seconds if provided. Iterations are unavoidable since it is a nonlinear problem. Number of iterations is dependent on the initial value supplied. In a dynamic simulation, using NLS solution from the previous time step as the initial value for the current time step is recommended as the initial value should be in the neighborhood of the actual solution, greatly decreasing the number of iterations. Combining this initial value strategy and providing analytical jacobians (instead of computing them numerically), a consistent solution time of 0.5−0.8 seconds was achieved.

SV and IMU experimental data collected during the Vicon benchmark test is used to further validate the accuracy of NLS. The rigid body translation and rotation are restricted, similar to numerical test cases. The INS measurements are not recorded and the NLS formulation is performed assuming a pinned boundary condition at the wing root. Therefore, the NLS fit will only be applicable for elastic states. Since the true strain state is unknown, the error metric for each time instant is defined by the difference between the Vicon IR markers and the displacement computed based on the NLS formulation at the same IR marker locations, that is:

$$r_V(t_k) = \frac{1}{n}\sum_{i=1}^{n}\left(\frac{d_{NLS}(t_k) - d_{Vicon}(t_k)}{b_{span}}\right) \tag{39}$$

This residue is then averaged over the entire time history, similar to what was done previously with the strain residue. Table 6 confirms the conclusion obtained from the numerical cases above. SV/IMU gives the best result in terms of displacement residue while the case with only IMU measurements gives the worst. The IR marker placed 2cm behind the LED Marker 1 is selected to provide quantitative data in the following discussion. Figure 17 and Figure 18 show that the displacement of this IR marker is well captured using SV information. From Figure 18, the roll angle recovered from the NLS matches the IMU and Vicon reading very well, however, the fit is deficient between the measured and recovered pitch angles. This suggests that less weightage should be given to the IMU readings in order not to force the NLS solution through the uncertainty in the measured IMU data. Figure 19 shows that the displacement error for the NLS solution with IMU increases as one moves from the wing root to the wing tip, unlike the situation with SV where there is no such trend.

Table 6. Displacement residue for Test Case 1 using NLS with various sensor combination. *Underlined cell indicates sensor combination with lowest residue.*

Measurements	Test Case 1 (% semispan)
IMU	−0.385
SV	0.0498
IMU/SV	$\underline{-0.0105}$

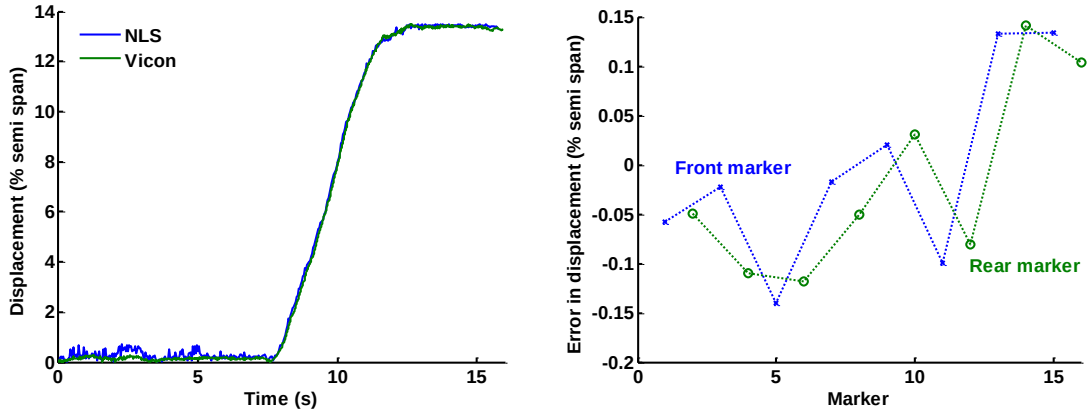

Figure 17. Displacement of IR marker recovered using NLS with SV information only (left). Spatial distribution of error using NLS (right).

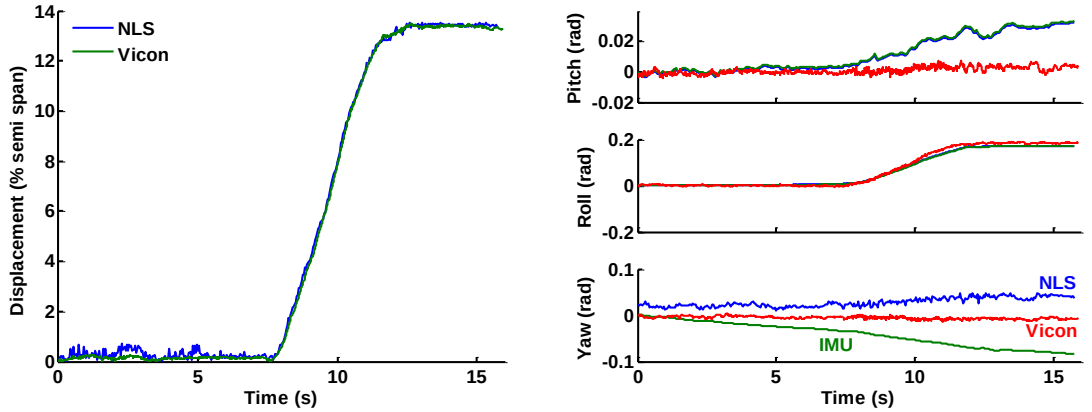

Figure 18. Displacement of IR marker recovered using SV+IMU information (left). Comparison of Euler angles of outboard IMU measured (IMU, Vicon) against NLS recovered solution (right)

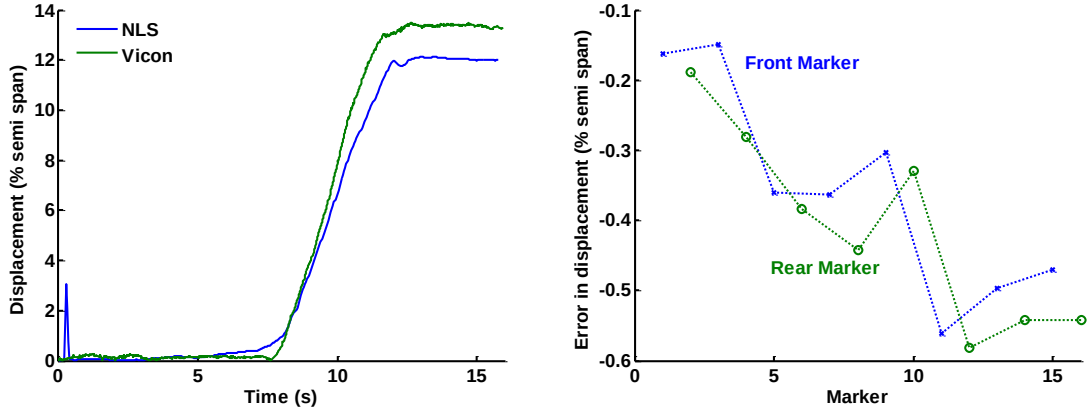

Figure 19. Displacement of IR marker recovered using IMU information (left). Spatial distribution of error using NLS (right).

C. Kalman Filter Accuracy

The continuous state space system shown in Eq. (12) is computed using UM/NAST. It is converted to discrete state space using zero-order-hold in MATLAB. The output equations Eq. (16) – (25) are differentiated to obtain linearized output C_d matrix. Sensor readings corrupted with noise are used as measurements and the control action is known and applied as input to the filter. The sensor noise covariance matrix is set to the variance of the sensor noise, i.e.,

$$R = \begin{bmatrix} \sigma_{\phi B}^{\ 2} & 0 & 0 \\ 0 & \ddots & 0 \\ 0 & 0 & \sigma_{pN}^{2} \end{bmatrix} \tag{40}$$

The selection of the process covariance noise should be tuned experimentally to achieve best results. It is tricky to define an analytical form as this process noise needs to account for higher order terms lost during the linearization process. Currently, it is set such that

$$Q = cI_{m\times m} \tag{41}$$

where c is a constant to be tuned and m is the number of input in state space equation. Figure 20 shows a value of c between 1 and 10 can be chosen as suitable noise covariance matrix magnitude. In all simulations below, c=1 is used.

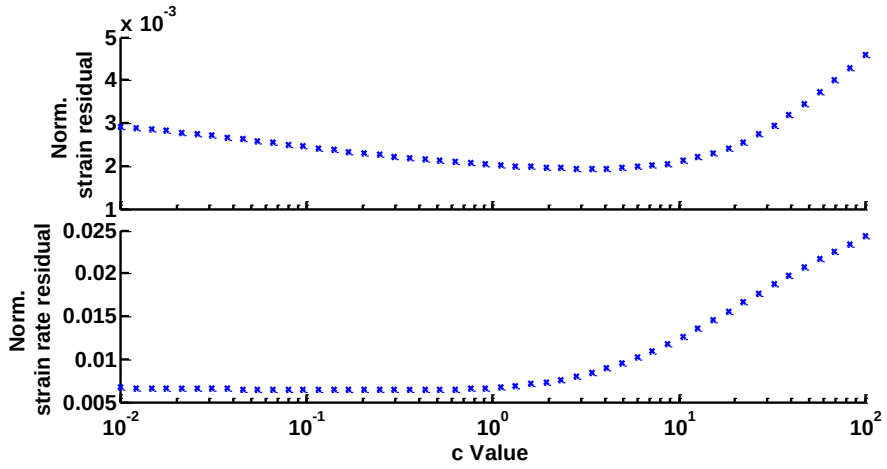

Figure 20. Plot of different values of noise covariance matrix Q against residue of strain and strain rate for Test Case 2.

Results in Table 7 show that the KF demonstrates comparable error regardless of sensor combination type. Figure 21 and Figure **22** show similar estimation using SV/IMU and IMU sensor sources. This can be attributed to two factors. Firstly, a linearized model of the system response is available, so if the system is observable, then the states can be reconstructed. Secondly, angular rates for all three axis are measured by the IMU gyroscope. All information is retained unlike in the NLS formulation where yaw angle information was discarded. The residue strain error is higher in the KF formulation compared to NLS when measurements are noiseless. This is due to the fact that NLS employs nonlinear relationship between strain and displacement while KF employs only a linearized relationship between strain and displacement. In the presence of noise in the measurements, the performance degrades compared to noiseless case. At the same time, it performs better than NLS. Again, this can be attributed to knowledge of system dynamics from the state space model. However, this is both an advantage and disadvantage. In the KF formulation, the input forces have to be known or measured. This information may not be always available (e.g., VFA encountering an unknown wind gust in the atmosphere).

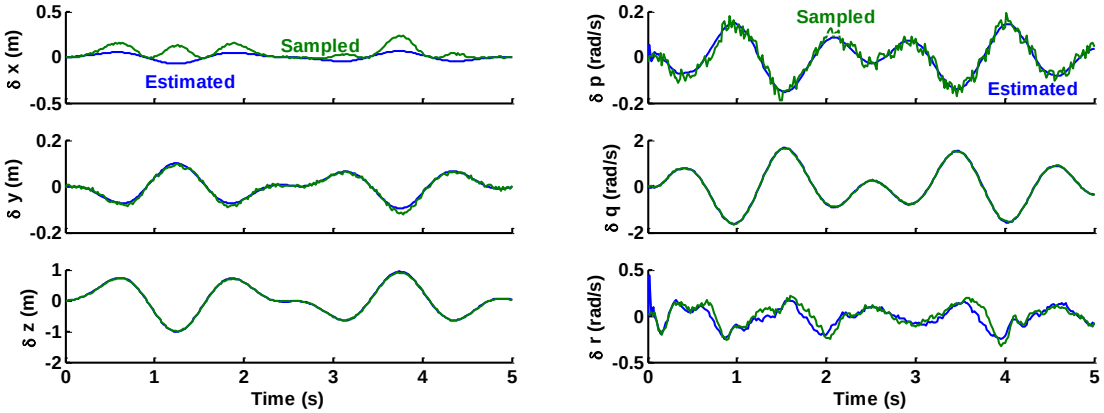

Figure 21. KF output of displacement components for Marker 18 (left). KF output of measured angular rates for left pod 1 (right). *Both figures show results from Test Case 2 using IMU/SV input corrupted with noise.*

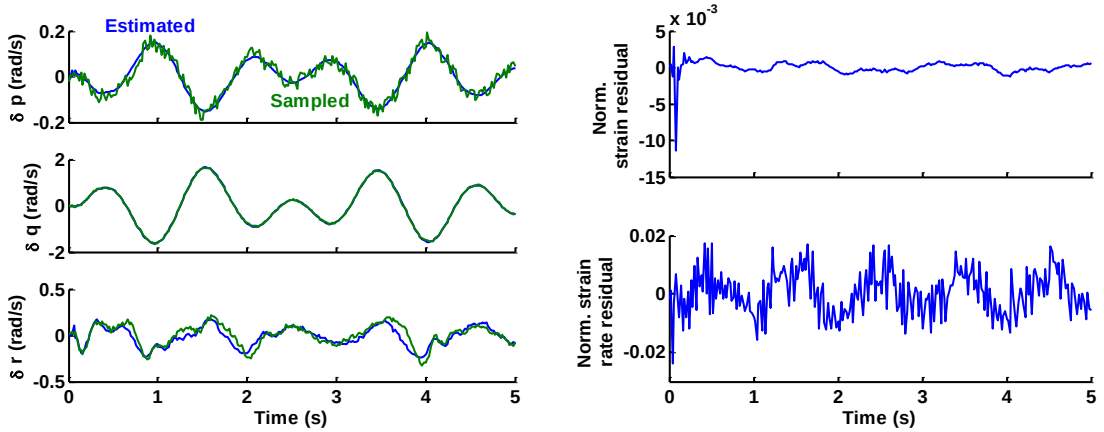

Figure 22**. KF output with measured angular rates for left pod 1 is shown (left). Time history of error residue (right).** *Both figures show results from Test Case 2 using only IMU input corrupted with noise.*

$\kappa_{max} = 0.437.\ \dot{\kappa}_{max} = 2.057$

Table 7. Strain residue r_ε using KF with various combination of measurement sources. *Underlined cells indicate sensor combination with lowest residue for each Test Case.*

Measurement	Test Case 2 (w/o noise)	Test Case 2 (with noise)	Test Case 3 (w/o noise)	Test Case 3 (with noise)	Test Case 4 (w/o noise)	Test Case 4 (with noise)
SV	-8.796×10^{-4}	-8.771×10^{-4}	-9.953×10^{-4}	-9.894×10^{-4}	-1.782×10^{-2}	-1.781×10^{-2}
IMU	-1.041×10^{-3}	$\underline{-2.003\times10^{-5}}$	$\underline{-5.439\times10^{-4}}$	1.835×10^{-3}	$\underline{-1.495\times10^{-2}}$	$\underline{-1.265\times10^{-2}}$
SV/IMU	$\underline{-6.640\times10^{-4}}$	3.214×10^{-4}	-2.787×10^{-3}	$\underline{-4.928\times10^{-4}}$	-1.588×10^{-2}	-1.347×10^{-2}

The time taken for one filter iteration computation is less than 0.001 seconds. This is due to the fact that discrete KF computation only requires matrix multiplications without the need for any iteration. As stated before, different sources of measurements will have different update rates. Simulating a realistic update of 50Hz for IMU and 1Hz for SV, and employing a multi-rate KF, the residue obtained is smaller compared to the IMU only case.

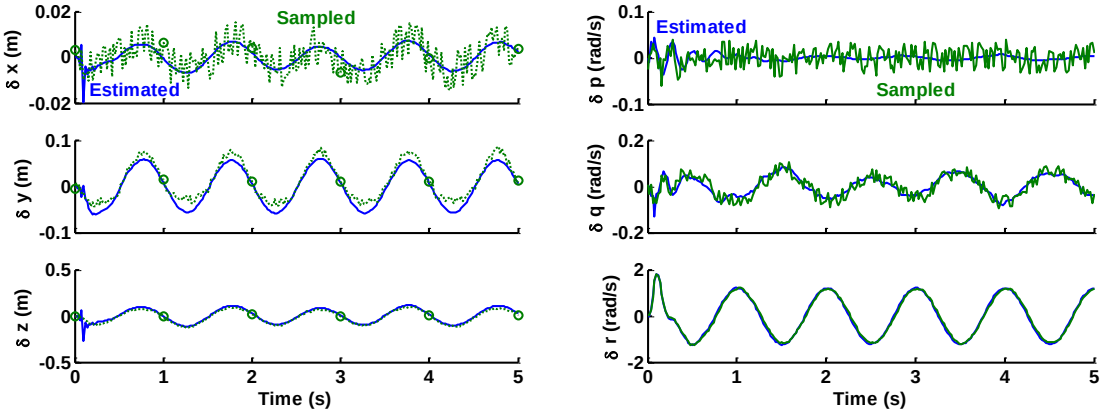

Figure 23. Multirate KF results for Test case 3 with IMU at 50Hz and SV at 1Hz. *Strain residue* $r_\varepsilon = 1.753\times10^{-3}$ *is better than IMU only case.*

In a realistic scenario, the input will not be known exactly due to measurement noise (e.g., noise in recording servo motor inputs on a VFA). On the other hand, the exact dynamics of the control may not be known (e.g., computing aerodynamic forces resulting from control surface deflection). To investigate this, the control input to the filter is corrupted with 10% max amplitude white noise and 10% bias for Test Case 2. Figure 24 shows good tracking using KF despite the uncertainty in input with a residue magnitude comparable to that where there is no uncertainty in the input.

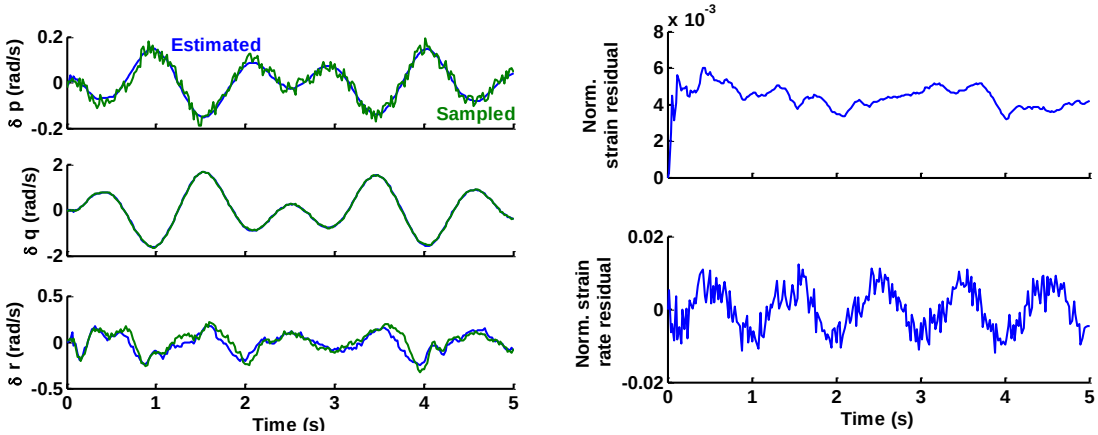

Figure 24. KF filter for Test Case 2 with noisy IMU measurements and noisy input. *Strain residue* $r_\varepsilon = 9.983\times10^{-3}$ *and still shows good tracking.* $\kappa_{max} = 0.437$. $\dot{\kappa}_{max} = 2.057$

D. Summary of NLS and KF Methods

A summary of the advantages and disadvantages of the Nonlinear Least Squares (NLS) and Kalman Filter (KF) formulations are summarized in Table 8 and Table 9 respectively.

Table 8. Summary of NLS characteristics.

Advantages	Disadvantages
- Nonlinear strain-displacement relationship (more accurate for large deformation) - No assumptions/knowledge about physical aircraft (mass/inertia/elastic properties). This is purely a kinematic fit - No assumptions/knowledge about control input	- Relatively slow computation (0.5 – 0.8s / snapshot) - Computation time varies due to required iteration steps - Requires all sensor measurements (INS/IMU/SV) at each snapshot. Rate limited by slowest sensor update rate - Accuracy degrades quickly in presence of noise in measurements

Table 9. Summary of KF characteristics.

Advantages	Disadvantages
- Fast computation (0.001s / snapshot) - Constant computation time since no iteration required - Allows multi-rate sensor measurements. Not rate-limited by sensor update rate	- Requires knowledge/assumptions about aircraft model (mass/inertia/elastic properties) - Requires knowledge/assumption of control excitation - Less accurate for large deformation (away from linearization point) due to higher order terms

V. Conclusions

This paper presented a method to determine the shape and attitude of a very flexible aircraft. The theoretical relationship among distributed IMU and stereovision (SV) markers on the wing surface to system states (elastic strain, elastic strain rate, body attitude, etc.) were presented. Then, two methods were proposed to estimate these states based on measurements. The first method is a nonlinear least squares (NLS) method using purely kinematic strain-displacement relationship. Using this method, it was shown that the full suite of sensors (INS/IMU/SV) is required to obtain good estimation. Experimental results indicated that a lower weight should be given to the IMU to prevent NLS from forcing the solution through noisy IMU data. The main advantage of NLS is that it does not require any knowledge of the system. The fit is based purely on strain-displacement kinematic relationship. However, at the same time, the inherent disadvantage is that sensor noise impacts greatly its accuracy. The second method employs a Kalman filter. The best performance is obtained using the full sensor suite, even though it is also able to provide good estimation with the IMU measurements only. This is useful in real-time application since SV marker information is expected to be rate limited. This can be attributed to knowledge of the system dynamics. The main advantage of this method is that it will be able to reject sensor noise. However, one must also have a fairly accurate model of the system. Lastly, KF performs much better in terms of computation time and complexity compared to NLS.

References

[1] Su, W., and Cesnik, C. E. S., "Nonlinear Aeroelasticity of a Very Flexible Blended-Wing-Body Aircraft," *Journal of Aircraft*, vol. 47, Sep. 2010, pp. 1539–1553.

[2] Raghavan, B., and Patil, M. J., "Flight Dynamics of High Aspect-Ratio Flying Wings: Effect of Large Trim Deformation," *Journal of Aircraft*, vol. 46, Aug. 2009, pp. 1808–1812.

[3] Noll, T. E., Brown, J. M., Perez-Davis, M. E., Ishmael, S. D., Tiffany, G. C., and Gaier, M., *Investigation of the Helios Prototype Aircraft Mishap. Volume 1: Mishap Report*, NASA Langley Research Center, Virginia: 2004.

[4] Cesnik, C. E. S., Palacios, R., and Reichenbach, E. Y., "Reexamined Structural Design Procedures for Very Flexible Aircraft," *Journal of Aircraft*, vol. 51, 2014, pp. 1580–1591.

[5] Dillsaver, M. J., Cesnik, C. E. S., and Kolmanovsky, I. V, "Gust Load Alleviation Control for Very Flexible Aircraft," *AIAA Atmospheric Flight Mechanics Conference*, Portland, Oregon: AIAA 2011-6368, 2011.

[6] Shearer, C. M., and Cesnik, C. E. S., "Trajectory Control for Very Flexible Aircraft," *Journal of Guidance, Control, and Dynamics*, vol. 31, Aug. 2008, pp. 340–357.

[7] Cook, R. G., Palacios, R., and Goulart, P., "Robust Gust Alleviation and Stabilization of Very Flexible Aircraft," *AIAA Journal*, vol. 51, Feb. 2013, pp. 330–340.

[8] Silvestre, F. J., and Paglione, P., "Dynamics and Control of a Flexible Aircraft," *Proceedings of the AIAA Atmospheric Flight Mechanics Conference and Exhibit*, Reston, Virigina: AIAA 2008-6876, 2008, pp. 1–18.

[9] Tuzcu, I., Marzocca, P., Cestino, E., Romeo, G., and Frulla, G., "Stability and Control of a High-Altitude, Long-Endurance UAV," *Journal of Guidance, Control, and Dynamics*, vol. 30, 2007, pp. 713–721.

[10] Qu, Z., Lavretsky, E., and Annaswamy, A. M., "An Adaptive Controller for Very Flexible Aircraft," *AIAA Guidance, Navigation, and Control (GNC) Conference*, Reston, Virginia: AIAA, 2013, pp. 1–11.

[11] Che, J., Gregory, I., and Cao, C., "Integrated Flight/Structural Mode Control for Very Flexible Aircraft Using L1 Adaptive Output Feedback Controller," *AIAA Guidance, Navigation, and Control Conference*, Minneapolis, Minnesota: AIAA, 2012, pp. 1–19.

[12] Baraniello, V. R., Cicala, M., and Cicala, L., "An Algorithm for Real Time Estimation of the Flexible UAV Structural Motions Using a Video-Based System," *14th International Conference on Information Fusion*, 2011, pp. 1–8.
[13] Lichter, M. D., and Dubowsky, S., "Shape, Motion, and Parameter Estimation of Large Flexible Space Structures using Range Images," *Proceedings of the 2005 IEEE International Conference on Robotics and Automation*, 2005, pp. 4476–4481.
[14] Bijker, J., and Steyn, W., "Kalman Filter Configurations for a Low-Cost Loosely Integrated Inertial Navigation System on an Airship," *Control Engineering Practice*, vol. 16, Dec. 2008, pp. 1509–1518.
[15] Meng, X., Dodson, A. H., and Roberts, G. W., "Detecting Bridge Dynamics with GPS and Triaxial Accelerometers," *Engineering Structures*, vol. 29, 2007, pp. 3178–3184.
[16] Cesnik, C. E. S., Senatore, P. J., Su, W., Atkins, E. M., and Shearer, C. M., "X-HALE: A Very Flexible Unmanned Aerial Vehicle for Nonlinear Aeroelastic Tests," *AIAA Journal*, vol. 50, Dec. 2012, pp. 2820–2833.
[17] Pang, Z. Y., Cesnik, C. E. S., and Atkins, E. M., "In-Flight Wing Deformation Measurement System for Small Unmanned Aerial Vehicles," *55th AIAA/ASME/ASCE/AHS/ASC Structures, Structural Dynamics, and Materials Conference*, National Harbor, Maryland: AIAA 2014-0330, 2014, pp. 1–13.
[18] Durham, W., *Aircraft Flight Dynamics and Control*, Hoboken: Wiley, 2013.
[19] Kalman, R. E., and Bucy, R. S., "New Results in Linear Filtering and Prediction Theory," *Journal of Basic Engineering*, vol. 83, 1961, p. 95.
[20] Armesto, L., Chroust, S., Vincze, M., and Tornero, J., "Multi-Rate Fusion with Vision and Inertial Sensors," *IEEE International Conference on Robotics and Automation, 2004. Proceedings. ICRA '04. 2004*, vol. 1, 2004, pp. 193–199.